Draft version September 19, 2024
Typeset using LaTeX **twocolumn** style in AASTeX631

IBEX Observations of Elastic Scattering of Interstellar Helium by Solar Wind Particles

H. Islam,[1] N. Schwadron,[1] E. Möbius,[1] F. Rahmanifard,[1] J. M. Sokół,[2] A. Galli,[3] D. J. McComas,[4] P. Wurz,[3] S. A. Fuselier,[2,5] K. Fairchild,[1] and D. Heirtzler[1]

[1] *Physics Department, Space Science Center, University of New Hampshire, Durham, NH 03824, USA*
[2] *Southwest Research Institute, San Antonio, TX 78228, USA*
[3] *Physics Institute, University of Bern, Bern, 3012, Switzerland*
[4] *Department of Astrophysical Sciences, Princeton University, Princeton, NJ 08544, USA*
[5] *University of Texas at San Antonio, San Antonio, TX 78228, USA*

ABSTRACT

The IBEX-Lo instrument on the Interstellar Boundary Explorer (IBEX) mission observes primary and secondary interstellar helium in its 4 lowest energy steps. Observations of these helium populations have been systematically analyzed and compared to simulations using the analytic full integration of neutrals model (aFINM). A systematic difference is observed between the simulations and observations of secondary He during solar cycle (SC) 24. We show that elastic scattering of primary helium by solar wind protons, which redistributes atoms from the core of the flux distribution, provides an explanation of the observed divergence from simulations. We verify that elastic scattering forms a halo in the wings of the primary He distribution in the spin-angle direction. Correcting the simulation for the effects of elastic scattering requires an increase of the estimated density of primary helium compared to previous estimates by Ulysses/GAS. Thus, based on our analysis of IBEX observations and χ^2 minimization of simulation data that include the effects of elastic scattering, any estimation of neutral interstellar helium density at 1 AU by direct detection of the peak flux of neutral helium needs to be adjusted by $\sim 10\%$.

Keywords: Heliosphere (711) — Interstellar medium (847) — Solar activity (1475) — Solar wind (1534) — Photoionization (2060) — Pickup ions (827)

1. INTRODUCTION

The Sun produces the supersonic solar wind (SW), which flows out radially and inflates the volume of our heliosphere. The distant boundaries of our heliosphere are created through the interaction of the SW with the dilute partially ionized gas of the very local interstellar medium (VLISM), consisting of neutral atoms, such as H, He, N, O, and Ne, and a charged plasma part consisting of electrons, protons, and heavier ions (Frisch et al. 2010). The neutral atoms of the interstellar medium travel relatively unimpeded through the heliosphere. The particle densities are so low in the VLISM and in the solar wind that typical mean collisional free paths are typically 10's to 100's of AU.

The Interstellar Boundary Explorer (IBEX) is a small NASA explorer mission that has provided us a decade long observation of Interstellar Neutral (ISNs) and Energetic Neutral Atoms (ENAs) in the energy range 15 eV to 6 keV (McComas et al. 2009a). There are two ENA cameras on IBEX: IBEX-Lo which is senstive to neutral atoms in the energy ranges between 10 eV to 2 keV (Fuselier et al. 2009a) and IBEX-Hi in the energy range between 0.38 keV to 6 keV (Funsten et al. 2009). Since its launch and commissioning, IBEX has observed ISNs from the pristine interstellar medium and from the interaction zone of the heliospheric boundary and the surrounding VLISM.

ISNs are an efficient tool to analyse the characteristics of the interstellar medium and the interaction at the boundary. IBEX fundamentally observes three types of neutral atoms (a) pristine ISNs like Hydrogen, Helium, Oxygen and Neon, (b) secondary populations of ISNs, which are created through charge exchange between primary ISNs and plasma in the outer heliosheath, and (c) energetic neutral atoms created from solar wind ions that undergo charge exchange in the inner heliosheath (to produce the globally distributed flux of ENAs), and form the IBEX ribbon (McComas et al. 2009b; Schwadron et al. 2009; McComas et al. 2014). IBEX observes hydrogen in ESA step 1 and 2 (15, and 30

eV) and helium in ESA steps 1-4 (15, 30, 55, 110 eV). IBEX-Lo also observed Oxygen in ESA steps 5 and 6.

ISNs are unaffected by magnetic and electric fields. Inside the heliosphere, ISNs undergo charge exchange and photo-ionization by solar extreme ultraviolet (EUV) radiation and thereby create pick-up ions (PUI) that are carried away by the SW. The newly made PUIs mass load and slow the SW plasma as it travels out to the Termination Shock (TS). Beyond the TS, the inner heliosheath (IHS) is populated by accelerated PUIs as well as decelerated and deflected SW. The IHS plasma is separated from the interstellar medium by a tangential discontinuity called the HelioPause (HP).

Among all species, helium is the second most abundant element in the interstellar medium after hydrogen (He/H $\sim$ 10) and is the least prone to ionization due to its high ionization potential and very low cross-section for charge exchange with the SW ions. Consequently, helium has the highest intensity at 1 AU and serves as an exceptional tool for studying the physical properties of interstellar medium. The first detection of neutral interstellar helium began with sounding rockets (Weller & Meier 1974), followed by satellites (Paresce et al. 1973, 1974), both methods relying on absorption and re-emission of solar EUV by helium. The discovery of helium pickup ions (He^+) in the SW by Möbius et al. (1985) introduced a novel method for analyzing neutral helium via the direct detection of He^+.

The first direct detection of neutral interstellar helium was made by the GAS experiment onboard Ulysses (Witte et al. 1992). The analysis of the GAS/Ulysses observation set the standard for interstellar helium parameters (Witte et al. 1993; Witte 2004). The density was determined to be 0.015 ± 0.0028 cm^{-3}, which was obtained as a best fit across two different observation seasons where the photoionization rate ranged from 0.6 to 1.6 $\times 10^{-7}$s^{-1}. Charge exchange and electron impact ionization were disregarded due to their negligible contributions. This density estimation aligns closely with the estimation of Gloeckler & Geiss (2004), 0.0154 ± 0.0015 cm^{-3}, based on measurements of interstellar He^{++} PUIs. The interstellar plasma flow outside the HP contains an abundance of He^+ ions (Frisch & Slavin 2003) that charge exchange with neutral helium atoms and thereby create a secondary population of neutral helium, dubbed "the warm breeze" (Kubiak et al. 2014, 2016). The warm breeze is warmer, slower and also deflected from the interstellar primary flow. In the progression of each ISN season, IBEX-Lo first observes the secondary He in early December to Mid January, followed by the primary population from early February to mid-March. Then the signatures of hydrogen are prominent until end of May (Saul et al. 2012,?).

The Sun goes through an approximately 11-year cycle during which its activity varies between relatively low levels (solar minimum) of activity to higher levels (solar maximum). During solar maxima, both solar wind fluxes and solar radiation fluxes increase. EUV radiation, which is tied to the photoionization rate, nearly doubles during solar maxima. ISN He within the heliosphere is modulated primarily by photoionization, a pattern that is evident in IBEX-Lo observations throughout Solar Cycle (SC) 24, spanning from 2009 to 2019 (Swaczyna et al. 2022; Rahmanifard et al. 2019).

We analyze the temporal variation of the differential flux of primary and secondary helium. The flux of the primary helium population shows a gradual increase starting from 2015, while the flux of the secondary population appears higher than expected. The temporal variation of secondary helium turns out to be very sensitive to the primary helium contribution. during the solar maximum and then decreases. The variation of the photoionization rate over the solar cycle can explain partially the observed changes in the primary population (Swaczyna et al. 2022), but does not account for the changes in the secondary population. As a potential explanation, we investigate the effects associated with elastic scattering of primary helium by the solar wind (Gruntman 1986).

As detailed by Gruntman (2013), the inclusion of scattering and the redistribution of primary helium can be interpreted as a loss of counts in the core of the primary helium velocity distribution. Quantitatively, this loss is similar in nature but much weaker than the photoionization loss. A direct consequence of incorporating loss due to elastic scattering is the revision of the interstellar helium density derived from direct neutral He observations, as reported for the first time in this study.
In Section 2, we describe the observations used for this study. Then we outline the model used to compare observations with simulations in Section 3. A central quantity used throughout this study is a renormalization constant (A), which multiplies the amplitude of modeled He fluxes and is determined through χ^2 minimization. Section 4 details the temporal variation of the renormalization constants for primary and secondary helium. In order to explain the increase of renormalization factor for secondary helium we discuss elastic scattering of solar wind proton and interstellar helium and also compares theoretical predictions with observations in section 5. In section 6, we explain why incorporating scattering requires the density estimation of primary helium

and which previous studies require revision based on our findings. Finally, in Section 7, we discuss and conclude our results.

2. DATA

IBEX is a Sun pointing spinner that completes a full rotation approximately every 15 seconds, sweeping its field of view across a roughly fixed swath (roughly centered on a great circle that passes through the ecliptic poles) of the sky. The swath is divided into 60 bins each 6° wide. IBEX-Lo and IBEX-Hi, the two cameras on IBEX, detect neutral atoms by converting them into ions in the instruments, which are then filtered by energy-per-charge using traditional electrostatic deflection techniques. IBEX-Lo spans the energy range from 0.01 to 2 keV into 8 different logarithmically spaced energy channels. After a neutral atom passes through the IBEX-Lo collimator it hits the diamond-like conversion surface at a shallow ∼15°angle of incidence (Fuselier et al. 2009a; Wieser et al. 2005). Neutral atoms with high electron affinity, e.g. hydrogen and oxygen are converted into negative ions with a high probability. Conversely, as a noble gas, He does not produce a stable negative ion. However, it can produce ions by sputtering, predominantly H^-, C^- and O^- ions. The sputtered ions are selected, based on their energy, using the electrostatic analyzer (ESA). The ions that pass through the ESA are then drawn into the time-of-flight (TOF) chamber with an applied Post-Acceleration (PAC) voltage.

Inside the TOF chamber these particles hit the first carbon foil and release secondary electrons from the surface, which are guided to the microchannel plate (MCP), creating a "start-A" signal. Then the ions hit a second carbon foil and the emitted electrons trigger another "start-C" signal. Finally, the ion reaches the MCP generating a "stop-B" signal.

The MCP has 4 quadrants and the ion is collected in one of these. The position of detection determines the TOF3 delay time along the delay line. If an event has two or three valid time-of-flight (TOF) values, then it is referred to as a double event or triple event, respectively. Triple events that satisfy the condition where the sum of TOF0 and TOF3 equals the sum of TOF1 and TOF2 are known as golden triple events. These golden triple events are characterized by a signal-to-noise ratio (SNR) of 1000 at peak ISN He flow, making them the most reliable events for analysis.

We have used histogram binned (HB) data which are accumulated events in the 6° spin bin histogram. Each spin starts at −3° of the North Ecliptic Pole (NEP), which is determined by the Attitude Control System (ACS) onboard IBEX using a star tracker (Hłond et al. 2012). At times when the Moon or the Earth fall into the the field of view of the star tracker the attitude information is faulty, resulting in unreliable histogram data. Time tagged direct event (DE) data still can be used by de-spinning periods when the star tracker is faulty (Fuselier et al. 2009b). We have restricted the analyzed data to periods with no star tracker outages.

We have used non despun histogram binned data consisting of golden triple events only. Additionally we remove times when one of the following conditions occur (Galli et al. 2022):

1. IBEX is inside Earth's magnetosphere.
2. Earth or Moon is in the field of view of the IBEX-Lo collimator boresight.
3. A gain or threshold test is performed
4. Counts are larger than 4 in either ESA step 7 or 8 in any of the 64 spin histogram blocks.
5. The whole orbit is discarded if the same high count as above continues for more than 12 hours, which is approximately 48 histogram blocks.

The last two conditions are used to determine periods of higher backgrounds. The time periods free of these conditions, and thus suitable for scientific analysis for each orbit, will henceforth be referred to as "ISN best-times".

In the summer of 2012, orbit 168b, the PAC voltage was reduced to 7 kV from 16 kV after a discharge when the spacecraft came out of an eclipse. TOF Efficiencies are lower after orbit 168, but this reduced efficiency is known based on calibration, and accounted for.

The observations we are using in this study are in the spacecraft frame of reference and they are not Compton-Getting corrected or Survival Probability corrected, as used in Galli et al. (2023). However there are two corrections imposed upon the observations, as briefly described here.

Throughput Correction — Before orbit 168, higher PAC voltages caused substantial unwanted TOF3 events due to background electrons. The IBEX Central Electronic Unit (CEU) has a buffer system that can store two events while another event is being processed. If another event occurs during this time, it is not registered. Swaczyna et al. (2015) devised an analytical model that calculates the probability of such scenarios and provides a correction factor. This factor is a function of TOF rates monitored over six sectors (each sector covering 60 degrees) and the count rate for each 6-degree bin. Although these orbits are excluded from the calculation of the renormalization constant which will be described

Table 1: Orbits used in this study

Year	Primary Orbits	Secondary Orbits
2013	0194b, 0195a, 0195b	0189a, 0190a, 0191a, 0191b, 0192a, 0192b
2014	0235a, 0235b	0229a, 0230a, 0230b, 0231b, 0232a, 0232b
2015	0275a, 0275b	0269a, 0270b, 0271a, 0271b, 0272a
2016	0315a	0309a, 0309b, 0310a, 0310b, 0311a, 0311b, 0312b, 0313a
2017	0355a, 0355b	0350a, 0350b, 0351a, 0351b, 0352a, 0352b, 0353a
2018	0395b, 0396a	0389b, 0391a, 0391b, 0392a, 0392b, 0393b
2019	0435b, 0436a, 0436b	0430a, 0430b, 0431a, 0431b, 0432a, 0432b, 0433a, 0433b
2020	0476a, 0476b	0470a, 0470b, 0471a, 0472a, 0472b, 0473a, 0473b

later, they are used to compare the width of the peak ISN helium distribution in the spin angle with later years. Further details can be found in section 4.

Spin Angle offset — In 2016, starting with orbit 326a, a shift was observed in the ISN data after a star tracker anomaly, which essentially changed the pointing direction of the IBEX-Lo boresight by +0.6° Swaczyna et al. (2022). Before the anomaly the bin center for the 0^{th} bin was 0°, which changed to 0.6° after the shift. This anomaly changes the count rate slightly in each bin from the nominal binning. To compensate for the change a redistribution method has been applied over the spin bins by fitting a Gaussian curve. More details can be found in Rahmanifard et al. [2024]

2.1. *Orbit Selection*

The science observation period for IBEX commences in early October. The secondary population of helium becomes dominant when the ecliptic longitude of the IBEX spin axis (Earth Ecliptic Longitude +180°) is approximately 235° − 295° (Kubiak et al. 2016), starting in mid-November and concluding in mid-January. Consequently, for each ISN season, the secondary orbits span consecutive years; for instance, during the 2015 ISN season, the secondary population includes orbits from 2014 and 2015. Subsequently, primary interstellar helium dominates at approximately 335° until the end of February. However, in this study, we have limited our selection of primary helium to the range of 310° to 320°, where the maximum ISN He flux is detected. This restriction is applied to minimize the influence of secondary helium. Observations beyond this period are focused on ISN hydrogen (Galli et al. 2019), extending through mid-May and covering an ecliptic longitude of approximately 60°. Orbits used in this study are given in Table 1.

3. SIMULATION

The study of the ISN distribution function began in the 1960s and early 1970s, under the assumption that the interstellar medium is cold Fahr (1968); Blum & Fahr (1970); Axford (1972). By the late 1970s, researchers such as Fahr (1979), Thomas (1978), and Wu & Judge (1979) started to develop hot models that account for the distribution of interstellar hydrogen at finite temperatures. Building on the hot model, Lee et al. (2012, 2015) proposed an analytical model designed to calculate the distribution function of ISN He within the heliosphere, specifically adapted to IBEX observations. This model utilizes an analytic formulation to estimate the survival probability of neutrals based on the ionization rate and solar wind flux, assuming that the ionization rate is constant at a specific location and decreases with the inverse square of the distance from the Sun.

Schwadron et al. (2013) expanded on this analytical model by developing a numerical integration model. This model integrates the distribution function over the detailed response function of IBEX-Lo, comprising three parts: integration over the spin sector, the collimator, and energy. Detailed descriptions can be found in (Schwadron et al. 2013, 2015).

This model is applied during the optimal ISN data acquisition times. For each three-hour interval of ISN best-time, the model is run separately, and the average count rate is calculated. At the average ISN best-time position, the real-time spin axis is determined. Using input parameters for interstellar helium and hydrogen, the count rates are then calculated. The parameters used in the model are listed in Table 2

4. TEMPORAL VARIATION OF RENORMALIZATION CONSTANTS

Simulating observations by IBEX-Lo gives us an opportunity to study the modulation of the ISNs in the vicinity of the Sun. The simulated rate is proportional to the density of helium population ($n_{\text{He},\infty}$) in their source region and the survival probability (S_p) of the

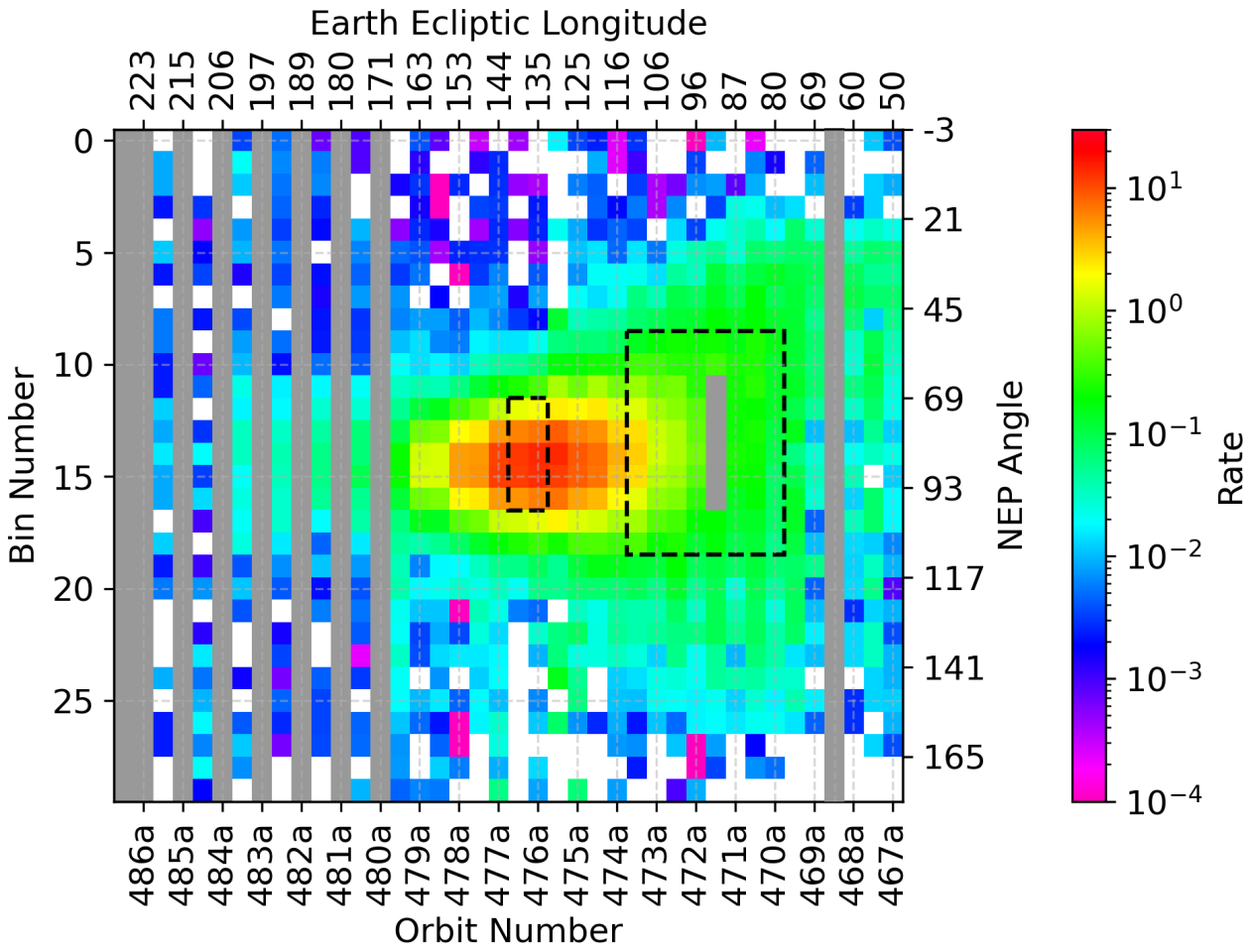

Figure 1: The data used for calculating the Renormalization Factor is presented using the ISN season 2019-2020 as an example. This plot demonstrates the selection of orbits based on Earth's Ecliptic Longitude and the NEP angle. The secondary orbits are chosen from 75° to 115° and bins 11 to 18, corresponding to a bin center angle range of 66° to 108° from the NEP. For the peak primary helium, the Earth's Ecliptic Longitude ranges from 130° to 140° and bins 12 to 16, corresponding to a bin center angle from 72° to 96° from the NEP. We have restricted our analysis to the selected region with the least amount of contribution by secondary helium. White pixels indicate a count of 0, while grey stripes denote the absence of valid good time for the selected bins (e.g., 471b) or the entire orbit (e.g., 468b).

Table 2:
Parameters for ISN He used in the Model

	Primary He	**Secondary He**
n_∞	0.00154 cm^{-3}	0.000878 cm^{-3}
T_∞	7500 K	9500 K
V_∞	25.4 km s^{-1}	11.3 km s^{-1}
λ_∞	75.75°	71.57°
β_∞	5.1°	11.95°

atoms. The survival probability is a function of the total loss rate which varies with the activity of the Sun based on the ionization rate. An important outcome of the comparison between observation and simulation is the renormalization constant (**A**), which is a factor multiplied to the modeled rate, derived in a chi-square minimum. The constant **A** acts as a scaling factor which essentially modifies the intensity of the simulated rate and is proportional to $n_\infty \times S_p$.

The temporal variation of **A** over the years provides direct insight into the ionization rate. Ideally, when the instrument's geometric factor, ionization rate, and density are accurately modeled, the renormalization constant should be 1. Assuming the geometric factor and density are precisely known, $\mathbf{A} > 1$ indicates an underestimated ionization rate, and $\mathbf{A} < 1$ suggests it is overestimated.

The loss of ISN He primarily due to photoionization. Extreme UltraViolet (EUV) radiation (~ 50 nm) from the sun is the primary source of ionization for ISN He. The intensity of the radiation varies between the maximum and minimum of each SC, over the period of approximately 11 years. We have applied an averaging scheme over the last part of the trajectory where the loss rate

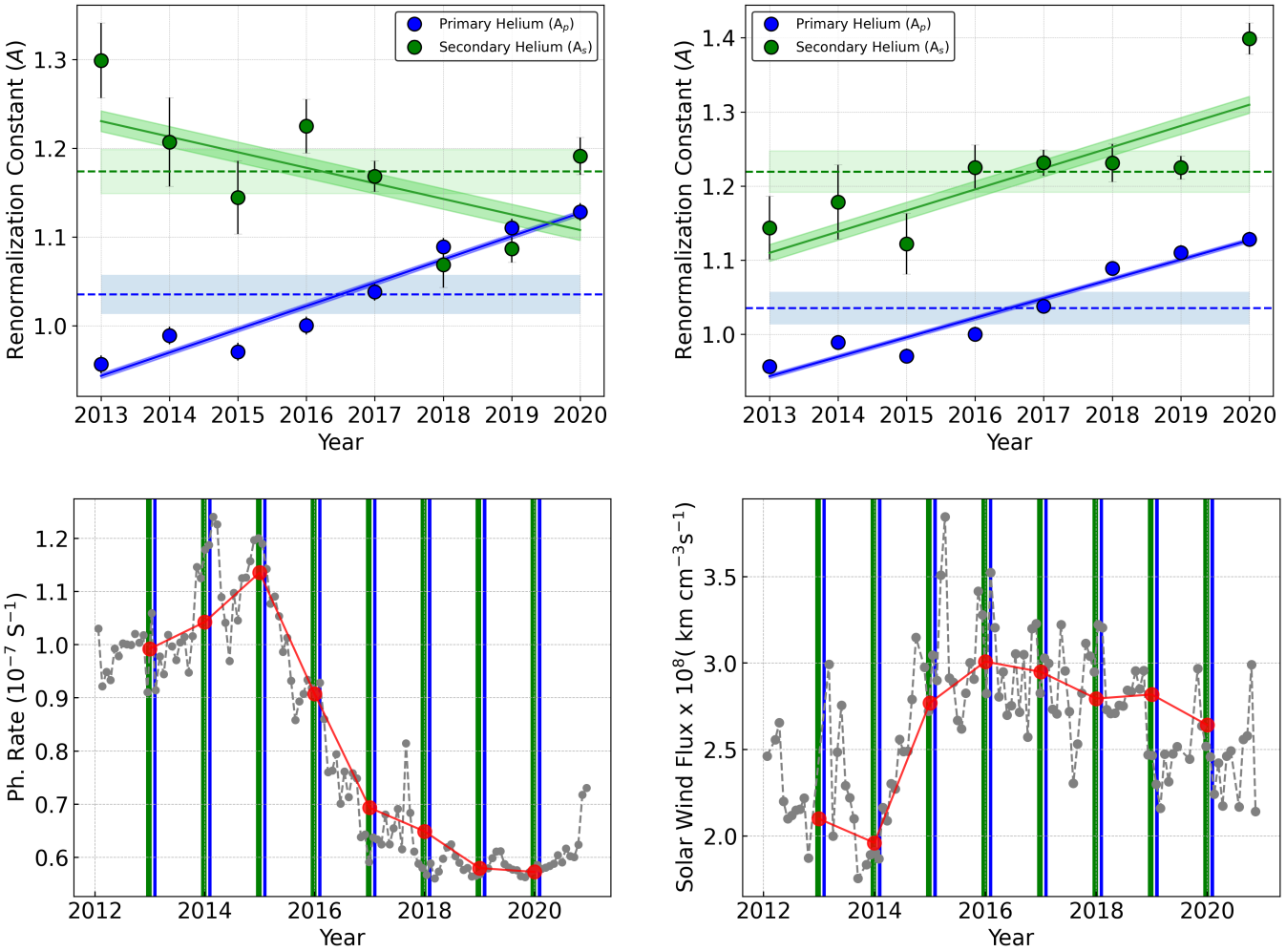

Figure 2: Shown are the renormalization constants for primary ($\mathbf{A}_p$) and secondary ($\mathbf{A}_s$) He obtained from aFINM with the temporal variation of the photoionization rate and solar wind flux for the years 2013 to 2020. *Top* – Blue and green filled circles represent $\mathbf{A}_p$ and $\mathbf{A}_s$ respectively. The solid blue line represents a time dependent linear fit for $\mathbf{A}_p$ which has a positive slope indicating that the renormalization constant increases with time. The dotted blue line with the light blue shaded region representing a 1σ error, is the time independent average of $\mathbf{A}_p$. Similarly the solid and dotted green lines, with their respective 1σ error, represent time dependent and independent fits over the years. We note an important observation - the trends for the two populations are opposite in nature. *Bottom left* – This panel shows temporal variation of the photoionization rate from 2012 to 2020. Light grey dots are the photoionization rate averaged over 1 Carrington rotation of $\sim$ 27 days. The green and blue shaded regions are times for which the secondary and primary orbits have been selected in this study. The red dots show the photoionization rate averaged over 7 Carrington rotations. *Bottom right* – This panel has the same structure as the left one representing the temporal variation of the solar wind flux. We note that the photoionization rate sharply decreases after the solar maximum in 2015 but the solar wind flux is almost constant from 2015.

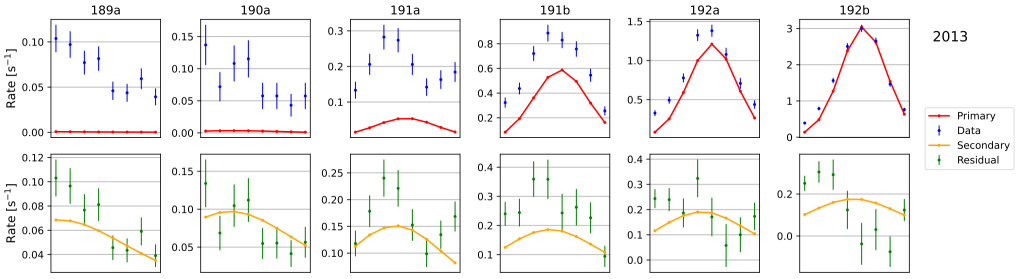

is higher than 10% of its value at 1 AU. The radius of the sphere of influence is approximately 4 AU from the sun and the time spent by ISN He inside this sphere is approximately 7 Carrington rotations of the sun (Rahmanifard et al. 2019) or $\sim$ 190 days. We neglect ionization of ISN He by charge exchange with SW protons, as

the cross section for charge exchange is very low (Sokół et al. 2020). We also neglect electron impact ionization because the radial dependence of electron impact ionization of ISN He is not well understood (Rucinski & Fahr 1989) and is not effective beyond 2 AU (Swaczyna et al. 2023).

The orbits used to estimate renormalization factors for secondary helium are shown in figure 3. For each year there are two rows, while each column represents unique orbit. In the upper panel, the blue dots represent the count rate observed by IBEX-Lo, while the red line denotes the simulated contribution from primary helium. The initial orbits, which are distant from the primary helium peak, show an almost negligible contribution from the primary population. Moving from left to right, as the orbits progress, the Earth's ecliptic longitude increases, leading to a corresponding rise in the contribution from primary helium. In the lower panel, the green dots show the residuals after subtracting the primary helium contribution from the observations. The yellow line represents the simulated secondary helium, which should aligns with the residuals. We calculate $\mathbf{A}_\mathrm{P}$ for primary helium and $\mathbf{A}_\mathrm{S}$ for secondary helium each year from 2013 to 2020. The reason for choosing these years are the following: (a) In summer of 2012 the Post Acceleration (PAC) Voltage was reduced to 7 kV from 16 kV. Due to the PAC voltage change, the efficiency of IBEX-Lo is reduced nearly by a factor of two (Swaczyna et al. 2023), which introduces an inconsistency into the temporal variation of A. (b) In the orbits where primary

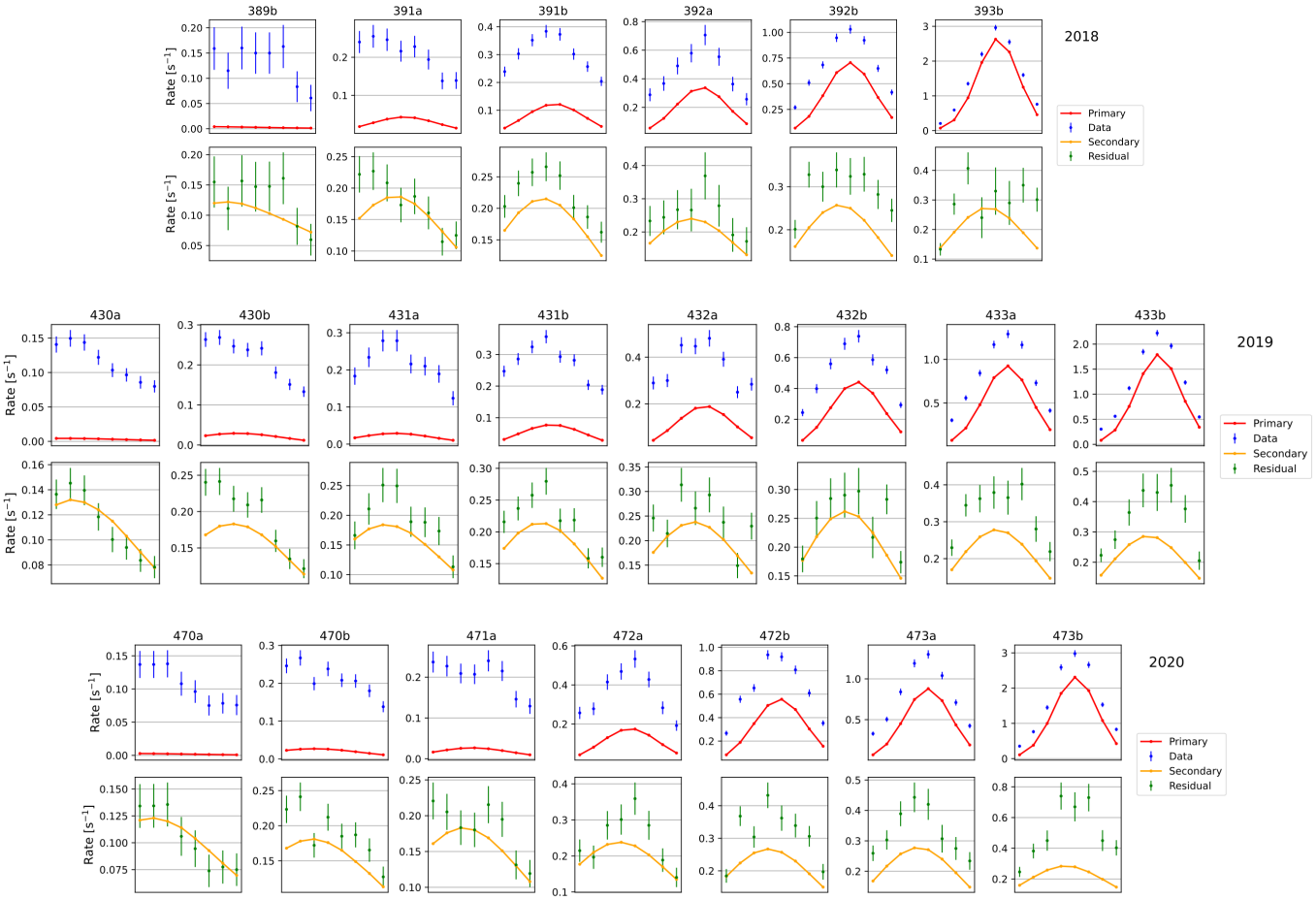

Figure 3: Count rates in different orbits for each year that are used to estimate $\mathbf{A}_s$. Each box represents a different orbit. The blue dots in the upper panel show the count rate observed by IBEX-Lo, while the red line represents the simulated primary helium contribution. The green dots in the bottom panel show the residual after subtracting the primary helium contribution from the observations. The yellow line indicates the simulated secondary helium, which is comparable to the residual. The data points correspond to the NEP spin angle (6° bin center) from 60° to 102°.

He is dominant, the contribution of secondary helium is negligible (the ratio of primary to secondary is approximately 30). However, the opposite is not true, thus we need to subtract the contribution of the primary population in the orbits dominated by the secondary helium. We will discuss later the effect of $\mathbf{A}_P$ on calculating $\mathbf{A}_S$. In 2011 and 2012 the primary helium data statistics is not substantial with the ISN best-time we have used in this study, subsequently these years are not included into the analysis. (c) Before orbit 130 in 2011, the orbits are longer in period $\sim$ 7.5 days. From orbit 130 the orbits are divided into arcs, each with a duration of $\sim$ 4.5 days. However, this change does not affect the analysis.

The top two panel of Figure 2 shows the temporal variation of $\mathbf{A}_p$ and $\mathbf{A}_s$. $\mathbf{A}_p$ remains almost constant from 2013 to 2015 (solar maxima) and gradually increases onwards. A time-dependent linear fit using years as a variable yields a positive slope of +0.02. The average value of $\mathbf{A}_p$ is found to be 1.04$\pm$0.02, indicating that the geometric factor used in the model is very close to the actual value. It is important to note that this geometric factor was derived assuming a primary helium density at infinity of $n_\infty = 0.0154\,\mathrm{cm}^{-3}$. Swaczyna et al. (2023) report similar findings from year 2009 to 2020 and argue that an overall 40% increase in the photoionization rate could explain this trend. However, the total uncertainty in the photoionization rate is at most 20%, rendering this assumption invalid. Another possibility considered was that the efficiency of IBEX-Lo is increasing over time, which is unrealistic. An unknown source at solar minima which is not present at the solar maxima may also explain the trend. The authors ultimately concluded that they could not resolve the matter.

As mentioned earlier, in peak primary orbits, the contribution of secondary helium is negligible, but this does not hold for secondary orbits. In the top left panel, $\mathbf{A}_s$ is calculated by multiplying $\mathbf{A}_p$ with the simulated pri-

mary helium rate before subtracting it from the data, whereas in the right panel, $\mathbf{A}_s$ is calculated without multiplying by $\mathbf{A}_p$. The trend of $\mathbf{A}_s$ in both panels is completely opposite, highlighting the strong influence of $\mathbf{A}_p$.

Unlike the primary helium, the renormalization constant for secondary helium, $\mathbf{A}_s$, in the left panel shows a negative slope of -0.01 ± 0.01, indicating a systematic decrease starting in 2013. The time-independent average value of $\mathbf{A}_s$ is significantly higher at 1.15 ± 0.02, suggesting that the count rate of secondary helium is, on average, 15% greater than predicted by the model. Galli et al. (2022) also reported unexpectedly high ENA intensity in 2015. Although the connection between this ENA surge and ISN helium is not well established, it may be relevant.

In contrast, when $\mathbf{A}_s$ is calculated without including $\mathbf{A}_p$, the trend aligns more closely with that of primary helium, with a slope of 0.03 ± 0.01 and a time-independent average of 1.22 ± 0.03. Notably, $\mathbf{A}_s$ shows a sudden jump after 2015, remaining constant until 2019, with a substantial increase in 2020 compared to previous years.

The temporal variations of the photoionization rate and solar wind proton flux in the ecliptic plane at 1 AU are shown in the bottom left and right panels of Figure 2. The photoionization rate was significantly higher during 2013–2016 compared to subsequent years, and $\mathbf{A}_p$ reflects this trend, suggesting an underestimation of ionization loss. However, during this period, $\mathbf{A}_s$ in the left panel was higher than in 2018 and 2019, which seems counterintuitive. In the right panel, $\mathbf{A}_s$ increased after 2015 but remained constant, which also does not follow the photoionization rate trend.

An additional contribution to the secondary population during periods of higher solar activity could explain this anomaly. We suggest that the scattering of primary ISN helium by solar wind protons may be responsible for this increase. The bottom right panel of the figure shows the solar wind flux from 2012 to 2020, with a rapid increase in mid-2014 followed by a slow decrease. A visual inspection of this trend alongside the temporal variation of $\mathbf{A}_s$ reveals a correlation. In the next section, we will discuss the scattering mechanism and its correlation with solar wind flux.

5. SCATTERING INSIDE HELIOSPHERE

ISN helium experiences loss primarily due to photoionization by solar extreme ultraviolet (EUV) radiation, a well-understood process. A minor contribution to this loss also arises from charge exchange and electron impact ionization (Rucinski & Fahr 1989; Bzowski et al. 2013; Bochsler et al. 2014). However, another physical process alters the ballistic trajectory of ISN He, causing reduction of flux in the core of the distribution: elastic scattering by the solar wind. Brandt (1964) first highlighted the significance of interstellar helium scattering by the solar wind. Wallis (1975), Fahr (1979) and Fahr & Lay (1974) realized that the temperature of interstellar helium and hydrogen ought to increase by collisional heating. Originally this heating mechanism was treated as a continuous process of energy and momentum exchange inside the heliosphere (Wallis 1974, 1975; Wu & Judge 1979) In 1986, Gruntman (1986) pointed out that, given the number of collisions an interstellar neutral atom experiences throughout its trajectory, continuous energy transfer is not applicable in this scenario. He also concluded that most atoms will gain very little momentum, resulting in a very thin but long wing of the distribution. A quantitative assessment of this theory was not provided until 2013 (Gruntman 2013). Based on that work we argue that the increase of the secondary helium flux during solar maximum can be explained by the scattering of primary ISN He by SW protons for the following reason: In the ecliptic plane, IBEX-Lo observes the peak for ISN He at a "sweet spot" that occurs at 130°, measured from the Vernal Equinox in the downwind direction. The relevant angular range where scattered particles distinguish themselves from the peak extends from less than 100° to more than approximately 160°. The region near 100° is primarily influenced by secondary helium. The area around 160° is dominated by interstellar hydrogen and we predict similar increase of ISN hydrogen flux in that region.

The author also predicts that similar halo would also be seen in the plane perpendicular to the ecliptic plane. The top panel of Figure 5 in (Gruntman 2013) shows three curves, the blue curve represents the spin angle distribution without any collision, green is for multiple elastic collisions, and red for a single elastic collision assumption, which has been used in that study. The middle and bottom panels show the ratio of one-to-no-collision with the no-collision model.

As IBEX spins, it completes a full rotation approximately every 15 seconds, sweeping its field of view across a wide swath of the sky. A new spin starts when IBEX-Hi points toward −3° from the North Ecliptic Pole (NEP), which is 177° for IBEX-Lo. The primary ISN He flux core is observed at approximately 264°. Theoretically, the collision-produced halo dominates at angles larger than 30° to 35° from the core of the helium flux which corresponds to angles less than 235° and more

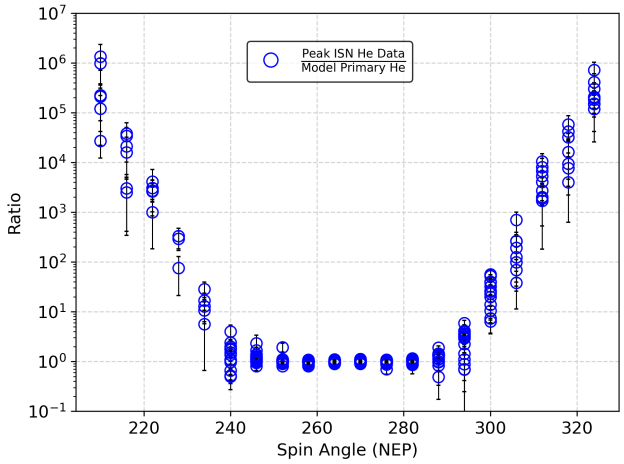

Figure 4: The helium flux halo observed by IBEX-Lo, which can be compared to the predicted ratio by Gruntman (2013). The primary helium orbits utilized in this study correspond to those specified in Table 1. Refer to the accompanying text for further details.

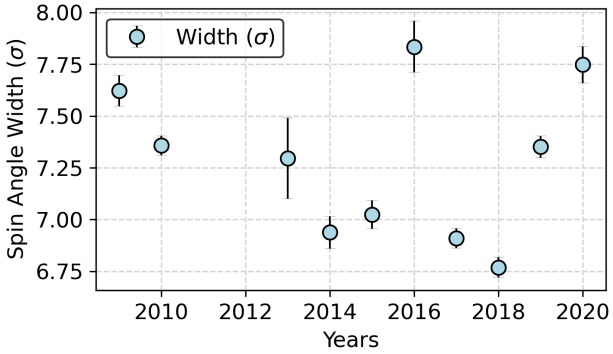

Figure 5: Width (σ) of the primary ISN He distribution in the latitudinal plane. The width is the standard deviation of the Gaussian Distribution fitted for the spin angle range 60° to 120°.

than 295° in the IBEX-Lo swath. To reproduce similar halo perpendicular to the ecliptic plane, we chose all the primary orbits used to calculate $A_P$and subtracted respective secondary helium from the observations. The simulated rate for primary helium serves as a conventional model without collision and the subtracted observation as the scattered distribution.

The theoretically predicted halo is also observed by IBEX-Lo as seen in Figure 4. The ratio between observation with the simulation is comparable to the middle panel of the said figure. Here we notice that at spin angle around 220 degrees the ratio is about 20 but the observed ratio by IBEX-Lo is of the order of thousand, 50 times higher than that theoretically predicted ratio. This deviation can be explained by using a higher scattering cross section. In the analytical model scattering cross section between Helium and solar wind protons is assumed to be 0.56×10^{-16}cm^2 at 450km/s with density 5cm^{-3}. In reality the solar wind density is higher and its speed fluctuates between 350-800 km/s. More specifically, the cross section falls off with increasing relative velocity between the interacting particles. Also, when the relative speed is lower the resulting scattering angle is higher. Thus, a higher cross section with higher scattering angle from a relative lower speed may explain the deviation but that analysis is beyond the scope of this work. (Gruntman 1986).

In SC 24 the SW flux increased by 50% in 2015 over the previous years and decreases slowly. It is intuitive to anticipate that the scattering phenomena will result in a broadening of the particle distribution in the spin-angle plane perpendicular to the ecliptic plane when the SW flux is higher. However, observations from IBEX-Lo reveal an inverse tendency, as shown in Figure 5. With the notable exception of 2016,2017,2018 particle distributions exhibit a narrowing effect during the solar maximum (2013,2014,2015) and a broadening effect during the solar minimum (2009, 2010, 2019, and 2020).A possible explanation is that, during solar maximum, the solar wind flux at higher latitudes is greater than in the ecliptic plane, leading to increased charge exchange between helium atoms and solar wind particles (Sokół et al. 2020). Additionally, the photoionization rate may be higher at elevated ecliptic latitudes during periods of high solar activity, further reducing the population of neutral particles available for scattering and subsequent detection. To verify these assumptions, a 3D ionization model that incorporates the ionization rate along with the trajectory of each particle is required which is beyond the scope of this work. The atypical broadening observed in 2016 can possibly be attributed to statistical anomalies (Swaczyna et al. 2022).

5.1. *Velocity Dependent Cross Section*

The elastic scattering cross section of proton and Helium atom is a function of energy. With increasing relative speed the cross section and the scattering angle both decreases. We have used the cross section data released by Swaczyna et al. (2021). The relevant speed range for the interaction between SW proton and helium is about 200 km/s to 1000 km/s. In this range we fit a power law equation

$$\sigma_{sc} = 3978.551 \times V_r^{-1.432} \quad (1)$$

to interpolate the scattering cross section for any relative speed, V_r. Based on the previous work by Gruntman (2013), we have assumed only 10% of the interaction leads to a scattering angle more than 1deg which is responsible for the halo formation.

5.2. *Correlation with the solar wind flux*

The observation of halo formation in primary helium orbits and the increased flux in secondary helium orbits confirm that the scattering effect is real and modifies IBEX observations. The temporal variation of secondary helium should exhibit a correlation between the scattering rate and the renormalization factors.

This correlation does not apply to the primary renormalization factor because the count rate for primary helium is significantly higher than the loss due to scattering, and uncertainties in the photoionization rate play a dominant role. When calculating $\mathbf{A}_{\mathrm{S}}$ subtracting the primary contribution from the data after multiplying it by $\mathbf{A}_{\mathrm{P}}$, assuming the same modulation applies across different orbits. However, the correlation between the scattering rate and $\mathbf{A}_{\mathrm{S}}$ was found to be -0.15, indicating almost no correlation. In contrast, when we subtract the primary contribution without multiplying by $\mathbf{A}_{\mathrm{P}}$, the correlation with the 452 days average scattering rate prior to the observation period is ~ 0.76, showing a strong correlation. This similarity between the renormalization factors and the scattering rate is visible in the Figure 2.

6. REVISED ESTIMATION OF INTERSTELLAR HELIUM DENSITY

Estimating the density, temperature, and velocity vector of ISN helium has been a key focus in interstellar medium studies over the past few decades. While the temperature and velocity vector of the ISN helium flow can be determined from the observed angular distribution, accurate instrument calibration is essential to determine the density in the pristine interstellar medium. Additionally, understanding the various filtration processes affecting helium atoms as they travel from the pristine interstellar medium to 1 au is fundamental. In a typical forward modeling approach, an initial density in the pristine interstellar medium is assumed, followed by applying the instrument response and accounting for the loss rate of the incoming flow.

The loss rate of helium atoms from the flux core due to elastic scattering by SW proton at heliocentric distance r is,

$$\beta_{sc}(r) = n_{\mathrm{p}}(r) v_{\mathrm{p}}(r) \sigma_{sc} \tag{2}$$

where $n_{\mathrm{p}(r)}$ and $v_{\mathrm{p}(r)}$ are the density and velocity of the solar wind protons and σ_{sc} is the scattering cross section. Loss rate by photoionization and elastic scattering both vary with the inverse square of the heliocentric distance. The total loss rate due to photoionization β_{ph} and scattering β_{sc} at any r is,

$$\beta(r) = \big(\beta_{ph}(r_E) + \beta_{sc}(r_E)\big) \left(\frac{r_E}{r}^2\right) \tag{3}$$

where r_E is the distance of the Earth from the Sun, *i.e.* 1 au.

The intensity of the helium count rate R obtained by forward modeling is directly proportional to the geometric factor of the instrument G, the density of helium in the pristine interstellar medium ($\mathrm{n}_{He,\infty}$) and the survival probability of the neutral helium along its trajectory (S_p),

$$R \propto G \times \mathrm{S}_p \times \mathrm{n}_{\mathrm{He},\infty}. \tag{4}$$

The survival probability of a neutral atom (Rucinski et al. 2003) is defined by

$$S_p(r(t)) = \exp\left[-\int_{t_s}^{t_r} \beta(r(t), t)\, dt\right], \tag{5}$$

where t_s is the starting time when ionization is relevant, t_r is the time when the atom reaches r, certainly $t_s < t_r$. $\beta(r(t))$ is total ionization rate at heliocentric distance r. The analytical solution (Lee et al. 2012) of the above equation assuming a constant ionization rate at distance r from the sun is

$$S_p(r) = \exp\left[-\frac{\beta(r) r^2 \Delta\theta}{L}\right], \tag{6}$$

where L is the angular momentum and $\Delta\theta$ is the angle swept out by the atom from infinity to r. A change in loss rate affects the estimation of S_p and subsequently $n_{\mathrm{He},\infty}$. In the simulation of different loss rates, the same count rate R can be obtained by simultaneously adjusting S_p and n_∞. From Equation 2 it is straightforward to obtain,

$$n^2_{\mathrm{He},\infty} = n^1_{\mathrm{He},\infty} \frac{S^1_p}{S^2_p}, \tag{7}$$

which reduces to

$$n^2_{\mathrm{He},\infty} = n^1_{\mathrm{He},\infty} \exp\left[\frac{r^2 \Delta\theta \Delta\beta}{L}\right], \tag{8}$$

where $\Delta\beta$ is the change in the loss rate. An increase in the loss rate suggests $\Delta\beta > 0$ resulting $n^2_{\mathrm{He},\infty} > n^1_{\mathrm{He},\infty}$ and vice-versa.

Inside the heliosphere, the scattering of ISN helium by SW protons is a source for the redistribution of ISN helium from the core of the distribution, which reduces the intensity of the observed flux. Thus, this mechanism should be accounted for along with the other ionization loss of He, effectively increasing the total loss rate. The exponential term in equation 8 represents the correction factor that adjusts the previously estimated density. In this work, we assume the bulk velocity of helium atoms in the pristine interstellar medium to be approximately 26 km/s, allowing us to calculate the angular momentum L and the angular deflection $\Delta\theta(r)$. With these

Table 3:
Revised Density of Interstellar Neutral Helium in the Pristine Interstellar Medium [$n_{He,\infty}$] for the inclusion of Scattering Loss and Warm Breeze Production

Previous Studies	**Density (cm^{-3})** [$\mathbf{n}_{He,\infty}$]	**Correction** Scattering Warm Breeze	**Revised Density (cm^{-3})** [$\mathbf{n}_{He,\infty}$]	**Methodology (Instrument)**
Vallerga et al. (2004)	0.013 ± 0.003	NA	0.013 ± 0.003 (NA)	UV Backscatter (EUVE)
Gloeckler et al. (2004)	0.0151 ± 0.0015	NA	0.0151 ± 0.0015 (NA)	Pickup Ions (Ulysses SWICS)
Witte (2004)	0.015 ± 0.0028	1.034 ± 0.002 1.057 ± 0.004	0.0164 ± 0.0032	Direct Detection (Ulysses GAS)
Wood et al. (2015)[1]	$0.0162^{+0.0058}_{-0.0031}$	1.018 ± 0.001 1.057 ± 0.004	$0.0174^{+0.0062}_{-0.0033}$	Direct Detection (Ulysses GAS)
Combined Revised Density [2]	0.0148 ± 0.0020	NA	0.0153 ± 0.0011	·

[1] Estimated only for 2006-2007.
[2] Calculated using only top three studies.

values, the correction factor can be straightforwardly determined. We emphasize that scattering does not result in an actual loss of helium atoms, rather the atoms are redistributed far enough from the flux core.

The three primary methods used for studying the interstellar medium are: (1) EUV resonant backscattering at 584 Å for neutral helium (2) observation of He^+ pickup ions, and (3) direct detection of ISN helium by the GAS experiment onboard Ulysses. A coordinated effort by Möbius et al. (2004) to combine all three methods resulted in a density estimate of $n_{He,\infty} = 0.0148 \pm 0.0020$. The density estimated by the above mentioned studies assumed no filtration of neutral helium flow at the outer heliosheath creating warm breeze which was first discovered in 2014. Below, we will analyze which of the three methods requires revision to account for scattering and the Warm Breeze.

6.1. *Resonant Backscattering*

Once the ISN helium parameters (Temperature and Velocity vector) influencing the intensity distribution pattern are determined, the product $g_0 n_\infty$ can be derived as the ratio of the observed intensity to the predicted intensity from a model where $g_0 n_\infty = 1$ (Dalaudier et al. 1984), where the excitation factor g_0 represents the rate at which a helium atom at rest scatters photons at 1 AU and n_∞ is the density of helium in the interstellar medium. The excitation factor is defined as $g_0 = F_{\lambda 0}\sigma_{\lambda 0}$, where $F_{\lambda 0}$ is the solar line flux at $\lambda = 584$ Å, and $\sigma_{\lambda 0}$ is the cross section for scattering photons by helium at rest. Helium atoms moving at different speeds experience different resonance frequencies due to the Doppler shift, resulting in varying cross sections for photon scattering and consequently different excitation factors. As redistributed helium atoms from the flux core will also contribute to the resonance emission, this does not affect the density estimation. However, due to it's asymmetry in the velocity space relative to the primary component, the presence of secondary helium slightly alters the excitation factor g, leading to a minor change in the density estimation, as demonstrated in Figure 7. In the helium flux core, primary helium arrives at 1 AU at a 45-degree angle relative to the observer-sun line with a speed of approximately 35 km/s. For secondary helium, this speed is around 31 km/s. Due to the presence of secondary helium, the solar line flux F_λ is slightly overestimated, by about 7%. Since secondary helium constitutes only about 6% of the primary helium, the excitation factor is overestimated by approximately 0.4%, which has a negligible effect on the density estimation. Thus, the density estimated by this method is unaltered. Here we assume that the resonant scattering cross section is constant for both velocities.

6.2. *PUIs Observation by SWICS/Ulysses*

The density estimation by the SWICS instrument via He^{++} pickup ions is the most accurate method for estimating ISN helium density for two reasons. First, the observations are made far from the Sun, at around 5 AU, where the photoionization rate is negligible. The uncertainty in calculating the photoionization rate is a fundamental source of error in density estimation. Second, no absolute geometric factor calibration is required for the density estimation. The only free parameter involved in the calculation is the cross section for PUI

production, which is beyond the scope of this study. As the two populations of helium are responsible for the production of pickup ions in the inner heliosphere, no correction is needed for that purpose. Additionally, the redistributed helium is expected to generate pickup ions (PUIs) in a manner similar to primary helium.

6.3. *Direct Detection by GAS/Ulysses*

Prior to the observational verification of secondary helium, the scientific consensus was that, unlike ISN hydrogen, ISN helium did not interact with the boundary of the heliosphere. Consequently, the density estimates derived from direct detection were considered to reflect the density in the pristine interstellar medium. However, following the discovery of the Warm Breeze by Kubiak et al. (2014), it was determined that approximately 5.7% of ISN helium is indeed converted into secondary ISN helium. Given that the signal-to-noise ratio for ISN helium detected by Ulysses is at best around 5, it was not possible to observe the contributions from secondary helium and the redistributed flux of primary helium. Therefore, a 5.7% filtration correction must be included in the density estimation.

To incorporate scattering loss at first the location of the Ulysses spacecraft has to be determined for the relevant time period, followed by the solar wind parameters. Ulysses is the only spacecraft which orbits the sun in a plane almost perpendicular to the ecliptic. From the time of it's launch in 1990, Ulysses has made three fast latitude scans around the sun. The direct observation of helium data analyzed by Witte (2004) uses first two fast latitude scans around perihelion (1994/09-1996/08 and 2000/09-2002/08) and Wood et al. (2015) uses all three fast latitude scans including the last one (2006/09-2007/08) to estimate the density of ISN helium and other parameters. We revise the density estimation from Wood et al. (2015) only for the final scan to avoid giving disproportionate weight to the first two scans. Note that, the photoionization rate used by these authors are significantly higher than the other studies, consequently their estimated density is also higher. Based on Ulysses' location, we estimate the solar wind speed and density, with the values provided in 10-degree bins ranging from 90 degrees to -90 degrees. For any specific latitude, the average is taken between the neighboring upper and lower latitude bins. For instance, if the position is at 55 degrees, we take the average between 50 and 60 degrees. The scattering cross section is calculated using equation 1. Once the scattering cross section is determined, the scattering rate at a distance r from the Sun, the associated survival probability, and the correction factor f_{sc} are subsequently calculated as described in the previous section. We compute f_{sc} over the period during which the data was analyzed and determine the mean f_{sc}. The standard deviation of these values represents the error associated with the factor.Figure 6 illustrates Ulysses' position and various solar wind parameters at 1 AU from 1992 to 2008. The shaded gray regions indicate the periods of fast latitude scans. The top left panel shows Ulysses' latitude, while the subsequent bottom two panels display the solar wind proton density and speed at that latitude at 1 AU. The bottom left panel shows the elastic scattering cross section based on the velocity. From the solar wind proton density, speed, and cross section, the scattering rate is calculated, which is then adjusted according to Ulysses' heliocentric distance, as shown in the top right panel. The corresponding scattering rate at that distance is depicted in the next bottom panel. The following two panels display the survival probability of helium atoms and the correction factor, f_{sc}. The sharp increase of f_{sc} during the first three fast latitude scans is primarily due to the Ulysses passing through perihelion.

The newly revised density estimates from GAS/Ulysses, along with those from two other methods, are presented in Figure 8. The x-axis represents the distance from the Sun. The density estimated from resonant scattering of He 584Å is at 1 AU, while the pickup ion method provides estimates at 5 AU. The GAS/Ulysses density covers a range from 1.3 AU to 2.5 AU, but for clarity, these values are plotted near 2.5 AU. Previously estimated densities are marked by filled circles, and the revised estimates by filled diamonds. Möbius et al. (2004) reported a combined density of 0.0148 ± 0.002 from all three methods, reflecting the consolidated local interstellar medium parameters. After revising the GAS/Ulysses data, the updated combined density is 0.0153 ± 0.0011, which remains within the upper bound of the previously estimated combined density. The original and revised combined densities are depicted by red filled circles and diamonds, respectively.

In SC 24, the average scattering rate of ISN helium atoms by solar wind protons, which redistributes atoms from the flux core, is approximately $0.15\times10^{-7}\mathrm{s}^{-1}$. This results in an additional reduction in survival probability by 10%, which is a non-negligible effect. This additional loss implies that any estimation of ISN helium density via direct detection must account for redistribution loss.

7. DISCUSSION AND CONCLUSION

We analyzed the observations of primary and secondary interstellar neutral helium with IBEX-Lo and examined the temporal variation of $\mathbf{A}_\mathrm{p}$ and $\mathbf{A}_\mathrm{s}$ from 2013 to 2020 and found the same trend for primary he-

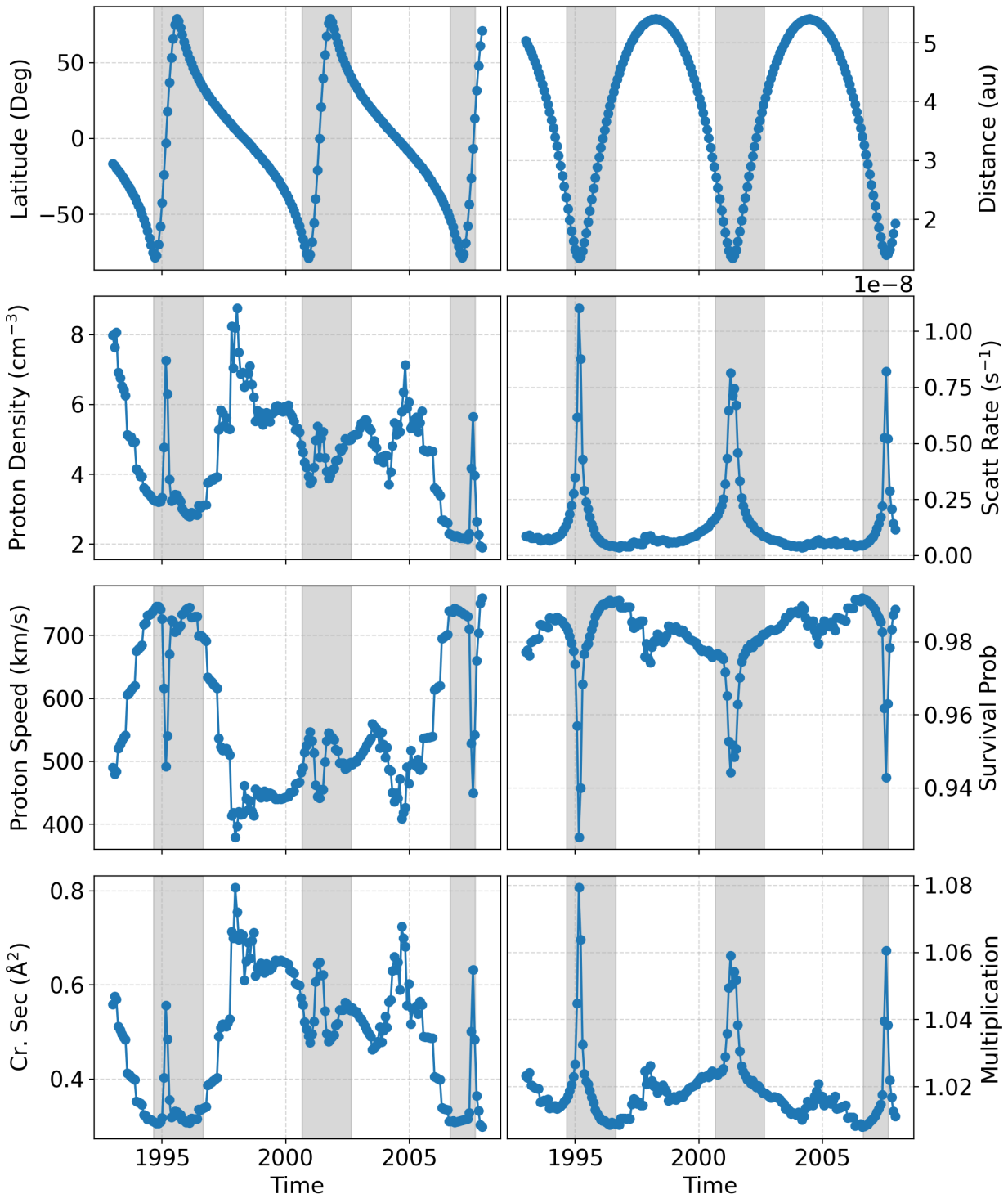

Figure 6: Position of the Ulysses spacecraft in the ecliptic coordinates , along with the different component of the solar wind and loss parameters of ISN helium. The two panels above give the latitude and heliocentric distance of Ulysses from the Sun. Gray-shaded regions represent the three periods of rapid latitude scans during which ISN helium was measured. During each of these three periods, Ulysses swept through near perihelion at high speed.Panel 2 and Panel 3 plot the solar wind proton density and velocity, respectively. The elastic scattering cross section as a function of relative velocity between protons and helium atoms is plotted in Panel 4. In Panel 6, we plot the rate of scattering loss and the corresponding survival probability in Panel 7.Panel 8 finally provides the correction factor, defined as the inverse of the survival probability. See the text below for a detailed explanation.

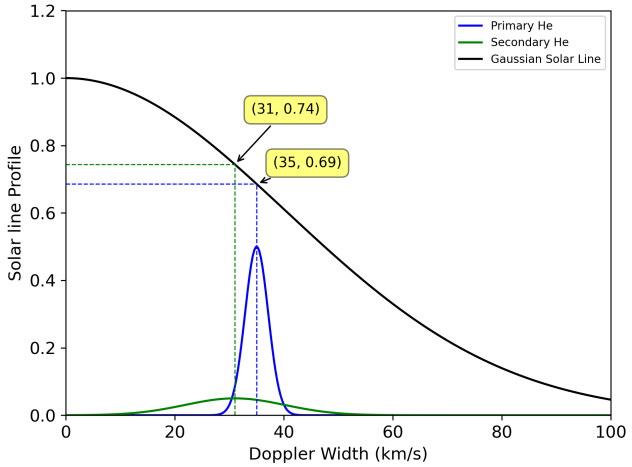

Figure 7: This figure illustrates the overestimation of the excitation factor g due to the presence of secondary helium. The wide, green Gaussian distribution representing secondary helium results in a higher excitation factor compared to the much narrower, solid blue distribution of primary helium. This difference is attributed to the lower velocity of secondary helium. The radial velocities of both helium populations are calculated at 1 AU, assuming an angle of 45° from perihelion. The solar line profile, depicted by the solid black line, demonstrates the variation in solar spectral line intensity across different Doppler velocities.

lium as reported by (Swaczyna et al. 2023), which is a gradual increase of $\mathbf{A}_\mathrm{p}$ from 2015 onwards. However, a systematic decrease in $\mathbf{A}_\mathrm{s}$ from the solar maximum is observed when $\mathbf{A}_\mathrm{p}$ is used (Figure 2). If $\mathbf{A}_\mathrm{p}$ is not included in the calculation of $\mathbf{A}_\mathrm{s}$, the trend reverses, becoming similar to the trend of $\mathbf{A}_\mathrm{p}$. For both of the cases a time independent average value of $\mathbf{A}_\mathrm{s}$ is 20% suggesting contribution from additional source.

We established that the scattering of interstellar helium by solar wind protons creates a halo, which naturally explains the increased flux of secondary helium. A higher correlation coefficient, when $\mathbf{A}_\mathrm{p}$ is excluded from the calculation of $\mathbf{A}_\mathrm{s}$, suggests that the primary helium population near the peak is not modulated in the same way as it is away from the peak.

We demonstrated that the density estimated from the direct detection of ISN helium by GAS/Ulysses needs to be revised to account loss by scattering as well as for the filtration of primary helium in the OHS, which contributes to the creation of the Warm Breeze. The scattering angle of ISN helium by solar wind protons depends on their relative speed; at higher speed, both the scattering cross section and scattering angle decreases, leading to very minor deviation from the original trajectory. The limitations of our analysis include the lack of velocity dependent scattering angle.Also, We assume that only 10% of the elastic scattering interaction produces an observable halo, and we calculate the scattering rate using the solar wind flux in the ecliptic plane at 1 AU. To enhance the robustness of this analysis, a comprehensive 3D model that tracks particle trajectories and incorporates the appropriate scattering rate is required.

In conclusion, the only methodology that requires revision for density estimation is the direct detection by the Ulysses GAS experiment.The revised combined density, based on earlier estimates, is calculated to be 0.0153 ± 0.0011. The original and revised values are provided in Table 3. Since the absolute geometric factor for IBEX was not determined with sufficient precision, accurate density estimation of ISN helium or hydrogen from IBEX-Lo observations is not feasible. However, future instruments like IMAP-Lo should be able to account for the scattering processes in more detail. If the loss in the helium flux core is considered, the core flux observed at 1 AU decreases by approximately 10%.

We thank all individuals associated with IBEX. We specially thank Paweł Swaczyna for many helpful discussions. This work is supported by the Interstellar Boundary Explorer mission as part of NASA's Explorer Program and partially by NASA SR&T Grant NNG06GD55G. JMS has been supported by NASA grant 80NSSC20K0719.

REFERENCES

Axford, W. I. 1972, in NASA Special Publication, ed. C. P. Sonett, P. J. Coleman, & J. M. Wilcox, Vol. 308, 609

Blum, P. W., & Fahr, H. J. 1970, A&A, 4, 280

Bochsler, P., Kucharek, H., Möbius, E., et al. 2014, ApJS, 210, 12, doi: 10.1088/0067-0049/210/1/12

Brandt, J. C. 1964, Icarus, 3, 253, doi: 10.1016/0019-1035(64)90021-1

Bzowski, M., Sokół, J. M., Kubiak, M. A., & Kucharek, H. 2013, A&A, 557, A50, doi: 10.1051/0004-6361/201321700

Dalaudier, F., Bertaux, J. L., Kurt, V. G., & Mironova, E. N. 1984, A&A, 134, 171

Fahr, H. J. 1968, Ap&SS, 2, 474, doi: 10.1007/BF02175923

—. 1979, A&A, 77, 101

Fahr, H. J., & Lay, G. 1974, in Space Research XIV, 567–573

Frisch, P. C., & Slavin, J. D. 2003, ApJ, 594, 844, doi: 10.1086/376689

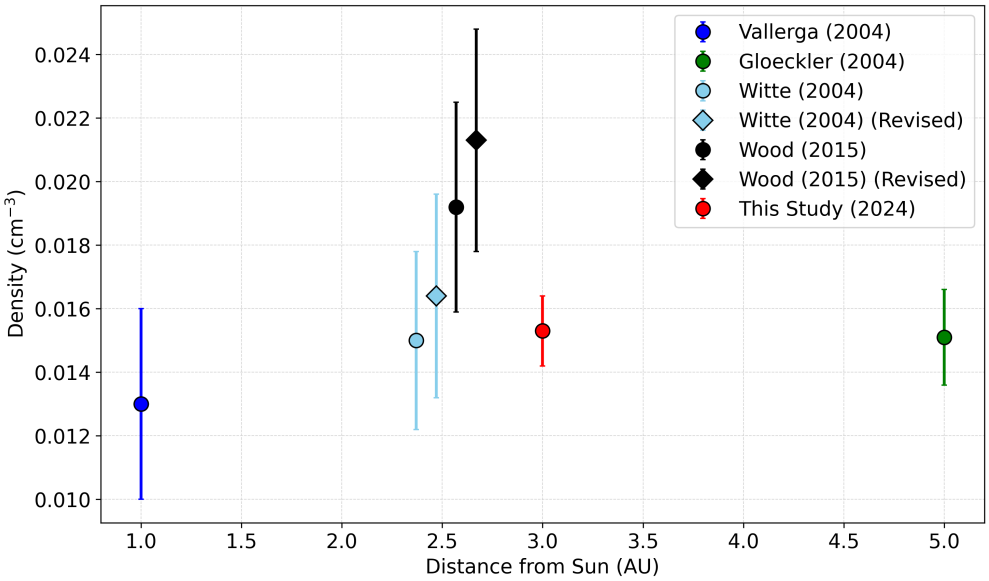

Figure 8: Reassessment of the previously estimated density by various studies. The density determined by Vallerga et al. (2004) and Gloeckler et al. (2004) remain unaltered. Revisions to the Ulysses/GAS estimations account for the influence of the warm breeze and scattering effects. The combined weighted average density estimated in this study is denoted by the red filled circle.

Frisch, P. C., Heerikhuisen, J., Pogorelov, N. V., et al. 2010, ApJ, 719, 1984, doi: 10.1088/0004-637X/719/2/1984

Funsten, H. O., Allegrini, F., Bochsler, P., et al. 2009, SSRv, 146, 75, doi: 10.1007/s11214-009-9504-y

Fuselier, S. A., Bochsler, P., Chornay, D., et al. 2009a, SSRv, 146, 117, doi: 10.1007/s11214-009-9495-8

—. 2009b, 146, 117, doi: 10.1007/s11214-009-9495-8

Galli, A., Wurz, P., Rahmanifard, F., et al. 2019, ApJ, 871, 52, doi: 10.3847/1538-4357/aaf737

Galli, A., Wurz, P., Schwadron, N. A., et al. 2022, ApJS, 261, 18, doi: 10.3847/1538-4365/ac69c9

Galli, A., Baliukin, I. I., Kornbleuth, M., et al. 2023, ApJL, 954, L24, doi: 10.3847/2041-8213/aced9b

Gloeckler, G., & Geiss, J. 2004, Advances in Space Research, 34, 53, doi: 10.1016/j.asr.2003.02.054

Gloeckler, G., Möbius, E., Geiss, J., et al. 2004, A&A, 426, 845, doi: 10.1051/0004-6361:20035768

Gruntman, M. 2013, Journal of Geophysical Research: Space Physics, 118, 1366, doi: https://doi.org/10.1002/jgra.50199

Gruntman, M. A. 1986, Planet. Space Sci., 34, 387, doi: 10.1016/0032-0633(86)90145-5

Hłond, M., Bzowski, M., Möbius, E., et al. 2012, ApJS, 198, 9, doi: 10.1088/0067-0049/198/2/9

Kubiak, M. A., Bzowski, M., Sokół, J. M., et al. 2014, ApJS, 213, 29, doi: 10.1088/0067-0049/213/2/29

Kubiak, M. A., Swaczyna, P., Bzowski, M., et al. 2016, ApJS, 223, 25, doi: 10.3847/0067-0049/223/2/25

Lee, M. A., Kucharek, H., Möbius, E., et al. 2012, ApJS, 198, 10, doi: 10.1088/0067-0049/198/2/10

Lee, M. A., Möbius, E., & Leonard, T. W. 2015, ApJS, 220, 23, doi: 10.1088/0067-0049/220/2/23

McComas, D. J., Lewis, W. S., & Schwadron, N. A. 2014, Reviews of Geophysics, 52, 118, doi: 10.1002/2013RG000438

McComas, D. J., Allegrini, F., Bochsler, P., et al. 2009a, SSRv, 146, 11, doi: 10.1007/s11214-009-9499-4

—. 2009b, Science, 326, 959, doi: 10.1126/science.1180906

Möbius, E., Hovestadt, D., Klecker, B., et al. 1985, Nature, 318, 426, doi: 10.1038/318426a0

Möbius, E., Bzowski, M., Chalov, S., et al. 2004, A&A, 426, 897, doi: 10.1051/0004-6361:20035834

Paresce, F., Bowyer, S., & Kumar, S. 1973, ApJL, 183, L87, doi: 10.1086/181258

—. 1974, ApJL, 188, L71, doi: 10.1086/181435

Rahmanifard, F., Möbius, E., Schwadron, N. A., et al. 2019, ApJ, 887, 217, doi: 10.3847/1538-4357/ab58ce

Rucinski, D., Bzowski, M., & Fahr, H. J. 2003, Annales Geophysicae, 21, 1315, doi: 10.5194/angeo-21-1315-2003

Rucinski, D., & Fahr, H. J. 1989, A&A, 224, 290

Saul, L., Wurz, P., Rodriguez, D., et al. 2012, ApJS, 198, 14, doi: 10.1088/0067-0049/198/2/14

Schwadron, N. A., Bzowski, M., Crew, G. B., et al. 2009, Science, 326, 966, doi: 10.1126/science.1180986

Schwadron, N. A., Moebius, E., Kucharek, H., et al. 2013, ApJ, 775, 86, doi: 10.1088/0004-637X/775/2/86

Schwadron, N. A., Möbius, E., Leonard, T., et al. 2015, ApJS, 220, 25, doi: 10.1088/0067-0049/220/2/25

Sokół, J. M., McComas, D. J., Bzowski, M., & Tokumaru, M. 2020, ApJ, 897, 179, doi: 10.3847/1538-4357/ab99a4

Swaczyna, P., Rahmanifard, F., Zirnstein, E. J., McComas, D. J., & Heerikhuisen, J. 2021, ApJL, 911, L36, doi: 10.3847/2041-8213/abf436

Swaczyna, P., Bzowski, M., Kubiak, M. A., et al. 2015, ApJS, 220, 26, doi: 10.1088/0067-0049/220/2/26

Swaczyna, P., Kubiak, M. A., Bzowski, M., et al. 2022, ApJS, 259, 42, doi: 10.3847/1538-4365/ac4bde

Swaczyna, P., Bzowski, M., Heerikhuisen, J., et al. 2023, ApJ, 953, 107, doi: 10.3847/1538-4357/ace719

Thomas, G. E. 1978, Annual Review of Earth and Planetary Sciences, 6, 173, doi: 10.1146/annurev.ea.06.050178.001133

Vallerga, J., Lallement, R., Lemoine, M., Dalaudier, F., & McMullin, D. 2004, A&A, 426, 855, doi: 10.1051/0004-6361:20035887

Wallis, M. K. 1974, MNRAS, 167, 103, doi: 10.1093/mnras/167.1.103

—. 1975, Planet. Space Sci., 23, 419, doi: 10.1016/0032-0633(75)90116-6

Weller, C. S., & Meier, R. R. 1974, ApJ, 193, 471, doi: 10.1086/153182

Wieser, M., Wurz, P., Nemanich, R. J., & Fuselier, S. A. 2005, Journal of Applied Physics, 98, 034906, doi: 10.1063/1.1996855

Witte, M. 2004, A&A, 426, 835, doi: 10.1051/0004-6361:20035956

Witte, M., Rosenbauer, H., Banaszkiewicz, M., & Fahr, H. 1993, Advances in Space Research, 13, 121, doi: 10.1016/0273-1177(93)90401-V

Witte, M., Rosenbauer, H., Keppler, E., et al. 1992, A&AS, 92, 333

Wood, B. E., Müller, H.-R., & Witte, M. 2015, ApJ, 801, 62, doi: 10.1088/0004-637X/801/1/62

Wu, F. M., & Judge, D. L. 1979, ApJ, 231, 594, doi: 10.1086/157221